Fabrication of superhydrophobic surfaces for applications in total internal reflection effects

Chi Hieu Hoang, Tran Thuat Nguyen, Duc Quan Ho, Hanh Vi Le, Hoang Hai Nguyen

Fabrication of superhydrophobic surfaces for applications in total internal reflection effects

Hoang Chi Hieu[a], Nguyen Tran Thuat[b], Ho Duc Quan[b,c], Le Hanh Vi[b,d], Nguyen Hoang Hai[b,*]
[a] Faculty of Physics, VNU University of Science, 334 Nguyen Trai, Thanh Xuan, Hanoi, Vietnam
[b] Nano and Energy Center, VNU University of Science, 334 Nguyen Trai, Thanh Xuan, Hanoi, Vietnam
[c] School of Physical and Mathematical Sciences, Nanyang Technological University, Singapore 637371, Singapore
[d] University of Rennes, INSA Rennes, CNRS, Institute FOTON-UMR 6082, Rennes, France

March 24, 2023

Abstract

Superhydrophobic surfaces have attracted significant attention in the applied science community. This paper presents three different methods for fabricating superhydrophobic surfaces, which can be applied in liquid light guides with the total internal reflection effect playing a central role. The selective bi-polymer etching only produces a hydrophobic porous poly(methyl methacrylate) surface but is simple and versatile for use on an arbitrary surface. In metal-assisted chemical etching, wet etching of a silver layer on a silicon sample creates porous silicon with superhydrophobicity, characterized by a water contact angle of 160°. The metal-assisted chemical etching method modified with the presence of polystyrene nanoparticles further improved the water contact angle to 164° by creating a nanopillar silicon structure. The metal-assisted chemical etching methods are more complicated but can produce superhydrophobic surfaces with very high water contact angles. These results show that superhydrophobic surfaces fabricated by methods in this study can be used for total internal reflection effect at the interface between water with huge potential applications in liquid light guides.

Highlights

- Versatile selective polymer etching to produce a superhydrophobic layer on an arbitrary surface.

- Morphology replication of a silver layer into a silicon surface by a metal-assisted etching method.
- Ordered columnar structure fabricated by a microsphere-based lithography method for a very high contact angle superhydrophobic silicon surface.

Keywords

superhydrophobic surface, porous polymer, porous silicon, nano-pillar silicon, contact angle, silica, interface.

1 Introduction

The interaction between water drops and solid surfaces is an essential and well-studied matter due to various applications. An ability of a surface to get wet is called wettability. The surface energy of the liquid σ tends to decrease the surface of the droplets, whereas the work of adhesion W tends to increase that surface. These two factors compete with each other and determine whether the interaction is either wetting or non-wetting. The Young-Dupre equation relates the work of adhesion and the surface tension through the contact angle θ [1]

$$\cos\theta = \frac{W}{\sigma} - 1 \tag{1}$$

The contact angle stands for the liquid's contact angle on a solid surface, which presents the wettability: superhydrophilic ($0° < \theta \leq 10°$), hydrophilic ($10° < \theta \leq 90°$), hydrophobic ($90° < \theta \leq 150°$), superhydrophobic ($150° < \theta < 180°$). The superhydrophobicity of a surface (SHS) depends not only on the intrinsic properties but also on the morphology of the surface, i.e., the roughness. To explain the superhydrophobicity, the Cassie-Baxter model [2] proposed that the liquid droplet rests atop the roughness features and rests on a composite air-solid surface to average the free surface energies [3]. A water droplet touches only the tip of the peaks over a solid, and the air layers below do not let the droplet touch the substrate.

SHSs are attractive for biotechnology, medicine, and heat transfer [4, 5]. In nature, superhydrophobic surfaces exist, such as the surface of a lotus leaf, a colocasia esculenta leaf, or a rose petal [6, 7, 8]. Superhydrophobic surfaces can be used to reduce viscous friction [9], absorb sunlight [10], exchange heat [11], self-cleaning windows [4].

Fiber optic light guides have been invented for a long time and have shown tremendous usefulness in telecommunication. However, liquid light guides need more attention despite their vast potential application in energy efficiency solutions. Recently, SHS has the potential for a liquid light guide due to the presence of an air layer between the liquid and solid surfaces [12, 13]. The light guide uses total internal reflection (TIR) to propagate electromagnetic waves based on the surface of a higher index refractive material and a lower refractive

index one. SHS possesses a natural feature favorable for total internal reflection, i.e., an air layer between a liquid and a solid media. Liquid light guides use water as a core material with a higher refractive index and air as a cladding with a lower refractive index. The air layer is retained between the core water and the surface of the superhydrophobic material. Liquid light guides are not ideal for propagating light over a long distance because the waveguide loss is significant. They are, however, valid for a short distance. We have several patents for concentrating solar light that use liquid light guides to introduce indoor [14, 15]. Because the distance is about several meters, liquid light guides are proper candidates for being used in such systems.

A superhydrophobic surface can be in one of three states: the Wenzel state, the Cassie-Baxter state, or the transition between these two states [3]. For applications in liquid light guide, the interface between liquid and solid must be in a Cassie-Baxter state because a thin air layer separating the liquid and the solid phase plays a central role in TIR needed for liquid light guide. The contact angle of a water droplet in a Cassie-Baxter state is given by

$$\cos\theta_{\mathrm{CB}} = f(\cos\theta + 1) - 1 \tag{2}$$

where θ_{CB} is the contact angle of a Cassie-Baxter droplet, θ is the Young contact angle of a droplet on the flat surface (in Equation 2), and f is the solid-liquid fraction of the SHS [3]. Equation 2 is used subsequently in this paper for deducing f, thus revealing information about the morphology of SHS.

There are many methods to fabricate SHS: coating the surface of microspheres [16], etching to create porous silicon surfaces [17, 18], replicating superhydrophobic biological surfaces [10], photolithography-based micro/nanofabrication technology [9], coating a hydrophobic Teflon film on the surface of microstructure [19], spray coating [20], or porous polymer [21, 22]... To maintain TIR, the stability of the air layer is essential, which depends on several factors. A little surfactant, heat, or contaminant can cause this layer of air to be removed. For the air layer to persist, the superhydrophobic surface must be porous enough to hold as much air as possible. Among SHSs listed above, porous polymer and silicon surfaces seem to have a slight advantage since (i) they are easy to be fabricated, (ii) they have the potential to contain more air, and (iii) they are familiar materials. This paper reports three methods to fabricate various superhydrophobic surfaces, including a periodic micropillar structure.

2 Methods

We prepared three series of samples by different methods: selective bi-polymer etching to produce porous poly(methyl methacrylate) (PMMA) (denoted as series A), metal-assisted chemical etching (MACE) to obtain porous silicon (series B), and metal-assisted chemical etching combined with polystyrene nanospheres (MACE-PS) to make nanopillar silicon (series C).

2.1 Fabrication of porous PMMA

The selective bi-polymer etching was based on a wet chemical technique to produce porous (PMMA) surfaces. Briefly, a solid mixture of PMMA (molecular weight of 93.9 kg/mol) and polystyrene (PS) (molecular weight of 194.9 kg/mol) with a desired [PMMA]:[PMMA+PS] ratio $\gamma_{\rm pm}$ was dissolved in tetrahydrofuran (THF) with a total polymer concentration $\gamma_{\rm p}$ as shown in Table 1. The solution was spin-coated on glass substrates at room temperature, with the spin coating rotation $v_{\rm s}$ from 8K–10K rpm (revolutions per minute), then dipped in cyclohexane at 70°C for 20 min. The samples were kept in a clean box for 12 h before conducting characterization experiments [23, 24].

#	$v_{\rm s}$ (K rpm)	$\gamma_{\rm p}$ (%)	$\gamma_{\rm pm}$ (%)
A1	$1-10$	5	$10-50$
A2	$8-10$	7.5	$10-90$
A3	$8-10$	$5-15$	50

Table 1: Preparation conditions for making porous PMMA: spin coating rotation $v_{\rm s}$, polymer concentration $\gamma_{\rm p}$, [PMMA]:[PMMA+PS] ratio $\gamma_{\rm pm}$.

2.2 Fabrication of porous silicon

Metal-assisted chemical etching of silicon was performed by a 2-step method: (i) forming of a silver layer, (ii) wet etching of silicon [25, 26]. The silver layer was deposited on silicon substrates using a direct current magnetron sputtering with the following conditions: a power of 90 W, pressure of 7.5×10^{-3} torr, a flow rate of 20 sccm of argon, and sputtering time of 30 s. The sample was then annealed under a vacuum at 300°C for 45 to 60 min. For the wet etching of silicon assisted by silver, HF 4.8 M was added with H_2O_2 1.2 M or 0.12 M to make the etchant have an initial liquid volume ratio $[HF]/[H_2O_2] = 1/1$. Under the effect of silver, the silicon surface was etched, leaving a hydrophobic surface. After etching, all samples were rinsed with deionized (DI) water and dried under a nitrogen atmosphere.

#	d (nm)	$t_{\rm e}$ (min)	c (M)
B1	$5, 10, 15, 20, 30$	$15, 30, 45, 60$	0.12
B2	$5, 10, 15, 20, 30$	$15, 30, 45, 60$	1.2

Table 2: Preparation conditions for making MACE: Ag thickness d, etching time $t_{\rm e}$, H_2O_2 concentration c.

2.3 Fabrication of nanopillar silicon

Metal-assisted chemical etching combined with PS nanoparticles was used to produce samples in series C. Figure 1 shows a schematic diagram for fabricating

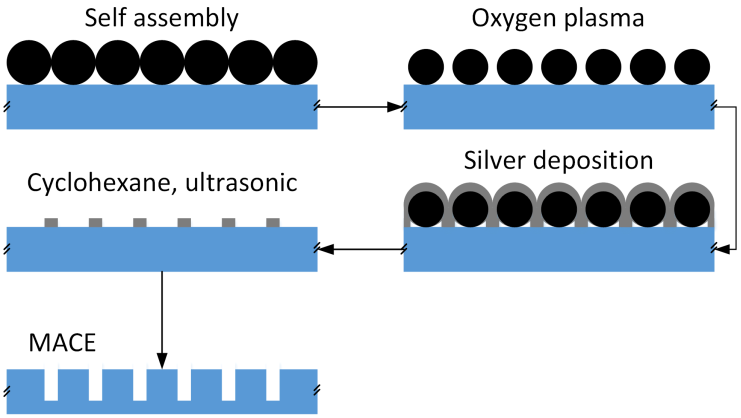

Figure 1: Schematic diagram for fabricating nanopillar structure of silicon in series C: (i) preparation of self-assembled hexagonal closed pack of PS nanoparticles on silicon surfaces, (ii) oxygen plasma etching of PS nanoparticles with desired remaining PS nanoparticles size, (iii) deposition of silver by a sputtering method, (iv) liftoff of PS nanoparticles in cyclohexane and ultrasonication, (v) MACE of silicon [27].

nanopillar structures: (i) preparation of self-assembled hexagonal closed pack of PS nanoparticles on silicon surfaces [27, 28, 29], (ii) oxygen plasma etching of PS nanoparticles with desired remaining PS nanoparticles dimension, (iii) deposition of silver by a sputtering method, (iv) liftoff of PS nanoparticles in cyclohexane and ultrasonication, (v) MACE of silicon [27, 30] followed by silver removal in an HNO_3 solution. Table 3 shows the main conditions for preparing silicon nanopillars. Details of this method are presented in the supporting information section.

#	r_p (nm)	t_e (min)	t_m (min)
C1	500	15	100
C2	800	$10-15-20$	$60-100$

Table 3: Preparation conditions for making silicon nanopillars: MACE time t_m, plasma etching time t_e, PMMA nanoparticle's initial radius r_p.

2.4 Contact angle measurement

To observe the hydrophobicity of a surface, we set up a simple system to take photos of water droplets on the surface. Among many methods for measuring the contact angle,[31, 32, 33, 34, 35] we have chosen the ImageJ software with LB-ADSA technique as a preloaded module [36]. The supplementary information gives details of the water angle measurement.

3 Results and discussion

The contact angle depends on the force between water and solid molecules at the microscopic level. These forces have electrostatic nature and can be classified in a decreasing strength interaction as (i) dipole–dipole (the interaction keeps water molecules liquid at ambient conditions), (ii) dipole–induced dipole (the interaction between water and oxygen, nitrogen molecules in air, water and PMMA, silicon/silica molecules), and (iii) induced dipole–induced dipole (the interaction between PMMA molecules). They are referred to as the Van der Waals interactions. The presence of silica may be due to the oxidation on the surface of silicon material. In any case, the interaction is dipole–induced dipole.

For water on the surface of PMMA, because the dipole–dipole interaction of water molecules, known as cohesion energy, is much stronger than the dipole–induced dipole interaction between water and PMMA molecules, known as adhesion energy, water tends to separate itself from PMMA. That makes the hydrophobicity of the PMMA surface. The situation is different with the silicon surface. It is well-known that silicon surface is quickly oxidized under ambient conditions to have a layer of silica. Silica is a hydrophilic material with a water contact angle of 20° due to a strong interaction of oxygen atoms in silica toward water [37, 38]. We need to modify the morphological structure of the surface to obtain superhydrophobicity, which aims to reduce the force between the water surface and the solid surface.

3.1 Porous PMMA

Figure 2 shows the dependence of water contact angle θ of series A1 on the preparation conditions shown in Table 1. Figure 2a shows that the contact angle changed from 80° to 140°. The highest θ of around 140° was obtained with the spin coating speed v_s from 8K rpm to 10K rpm and [PMMA]/[PMMA+PS] ratio, γ_{pm}, from 45% to 50%.

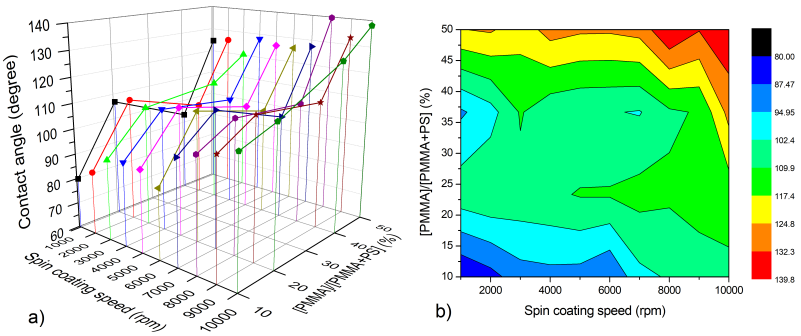

Figure 2: The dependence of the water contact angle on the polymer ratio γ_{pm} with $\gamma_p = 5\%$, spin-coating rotation speed v_s of samples in series A1.

Figure 3 shows the dependence of the water contact angle of series A2 and

series A3 on the preparation parameters γ_{pm} and γ_p. Large values of θ of around 140° occur at γ_{pm} of 50% to 70% and γ_p of 5.0% and 7.5%. The surface fabricated by this method is not good enough to be superhydrophobic but still suitable for making light guide tubes. This method is versatile since the polymer coating and etching can be done on any arbitrary surface. The contact angle value is higher than that reported in the literature by the same polymer-based method, typically of about 130°–144° [23, 24].

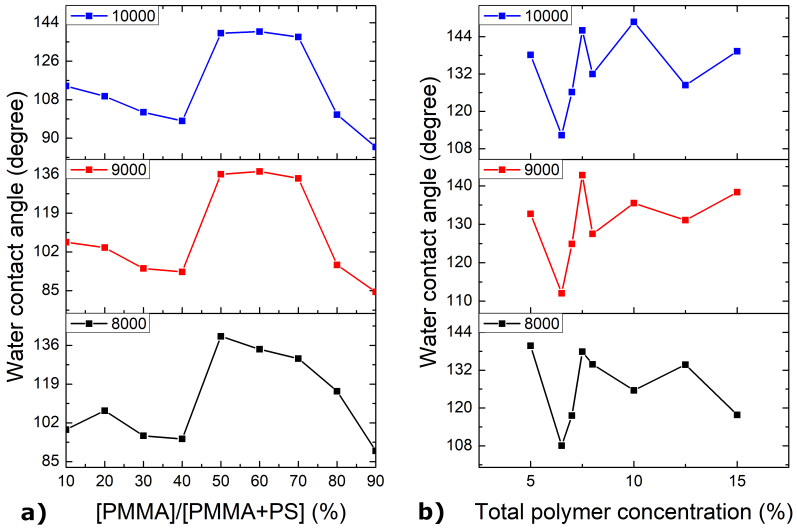

Figure 3: Dependence of water contact angle on γ_{pm} with $\gamma_p = 7.5\%$ (left) of samples in series A2 and on γ_p with $\gamma_{pm} = 50\%$ (right) of samples in series A3.

3.2 Porous silicon

Figure 4 and 5 shows the dependence of the water contact angle on porous silicon surfaces of samples in series B1 and B2 with the H_2O_2 concentration c of 0.12 M and 1.2 M, respectively. Preparation parameters varied with the initial silver thicknesses d from 5 nm to 30 nm and the etching time t_e from 15 to 60 min. The results revealed an increase of θ with t_e and a decrease with d for three series of samples with d = 5 nm, 25 nm, and 30 nm, whereas a slight decrease and increase are observed for two series with d = 10 nm and 15 nm. The highest contact angle, around 163°, was found for the silicon surface corresponding to the thinnest initial silver layer and the longest etching time of all investigated series. When the H_2O_2 centration was 1.2 M, getting an SHS with high contact angles was easier. SHS can be achieved with $d > 10$ nm and $t_e > 20$ min. The higher the H_2O_2 concentration, the easier to obtain an SHS since H_2O_2 plays the central role in oxidizing silicon, thus favoring the subsequent etching by HF. As the etching time increases, the water contact angle increases.

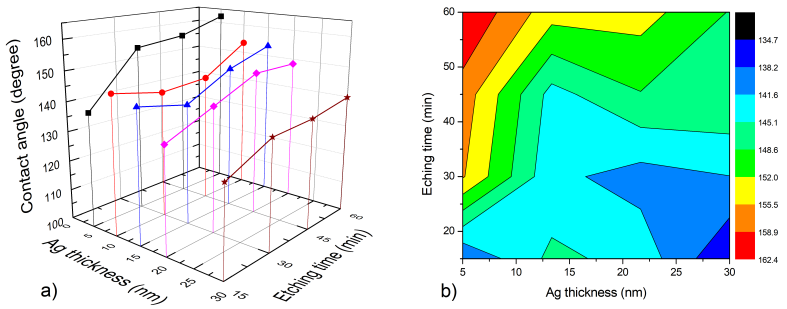

Figure 4: Dependence of the contact angle θ on the silver thicknesses t and the etching time t_e in samples of series B1 with the H_2O_2 concentration of 0.12 M.

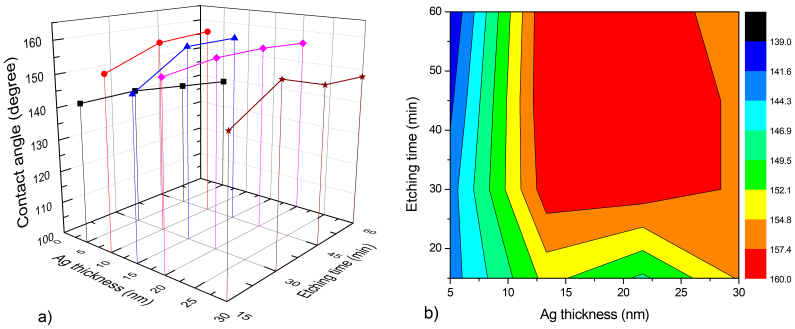

Figure 5: Dependence of the contact angle θ on the silver thicknesses t and the etching time t_e in samples of series B2 with the H_2O_2 concentration of 1.2 M.

Figure 7 presents the SEM images of the as-deposited silver after MACE of the sample in series B. Depending on the thickness of the silver layer, after annealing at 300°C, we obtained samples with two different morphologies. SEM images of the samples with $d = 5, 10$ nm show small spherical nanoparticles with a diameter of about 10 nm. For thicker silver layers, silver droplets appeared, which could come from the aggregation of many small nanoparticles. These two morphologies created two types of structures after etching. In the etched samples of series B1 with $c = 0.12$ M (the central column), the small spherical nanoparticles produced random porous surfaces, whereas the silver droplets created regular and flat porous surfaces. The random etching process yields porous silicon surfaces with a high water contact angle. In contrast, the regular and flat surfaces lead to a lower water contact angle. SHS appears in several samples with $d = 5$ nm and $t_e \geq 40$ min.

The situation differs in the etched samples in series B2 with $c = 1.2$ M (the right column). The contact angle gets the highest values for thick silver

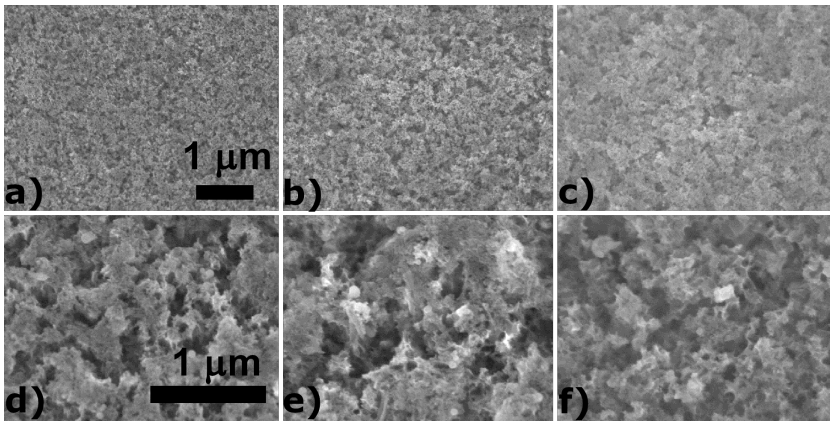

Figure 6: Surface morphology of porous silicon samples in series B2. The preparation conditions: $d = 5$ nm (top, a to c) and $d = 10$ nm (bottom, d to f); $t_{\mathrm{m}} = 15$ (left, a and d), 30 (middle, b and e), 45 min (right, c and f).

layers with etching time $t_{\mathrm{e}} \geq 30$ min. SHS occurs in almost samples with $d \geq 10$ nm because those samples have high roughness coming from the columnar morphology. Flattened (for $d = 5$ nm of silver) and broken (for $d = 30$ nm of silver) surfaces lead to a low water contact angle. Rough surfaces (for $d = 10$, 15, 20 nm) yield a high water contact angle. The result can be explained by the fact that series B1 had regular patterns, whereas series B2 did not. A previous study reported that the higher H_2O_2 concentration, the higher the etching rate [27]. For series B1, a lower H_2O_2 concentration, which is corresponded to a lower etching rate, leads to the regular patterns in series B1 [30]. Hence, a vertical etching process corresponds to replicating the etched silicon surface compared to the original silver surface. On the contrary, a high etching rate did not favor the silver particles or droplets to be immobilized. When the silver particles or droplets did not stay still, small movements would lead to broken columnar or random porous structures of the silicon surface, as observed for series B2.

The surface morphology change with the etching time shown on SEM images of the sample of series B2 with $c = 1.2$ M in Figure 6 explains the increase of θ with t_{e}. The surface of the samples with $d = 5$ nm did not change significantly as the etching time increased. They were porous but had a relatively flat surface. The contact angle depends on the porosity on the surface of the samples with $d = 10$ nm, which became significant with increasing etching time. The samples with $d = 5$ nm had smaller water contact angles than those with $d = 10$ nm. As the etching time increased, the water contact angle did not increase for $d = 5$ nm but slightly increased for the sample of $d = 10$ nm. One knows there is always a non-polar SiO_2 layer on any silicon surface under ambient conditions. We can create an SHS by controlling the morphology of a surface through its porosity. A high contact angle of 155°–160° has been achieved. The following section presents a method for increasing the interfacial air layer between water

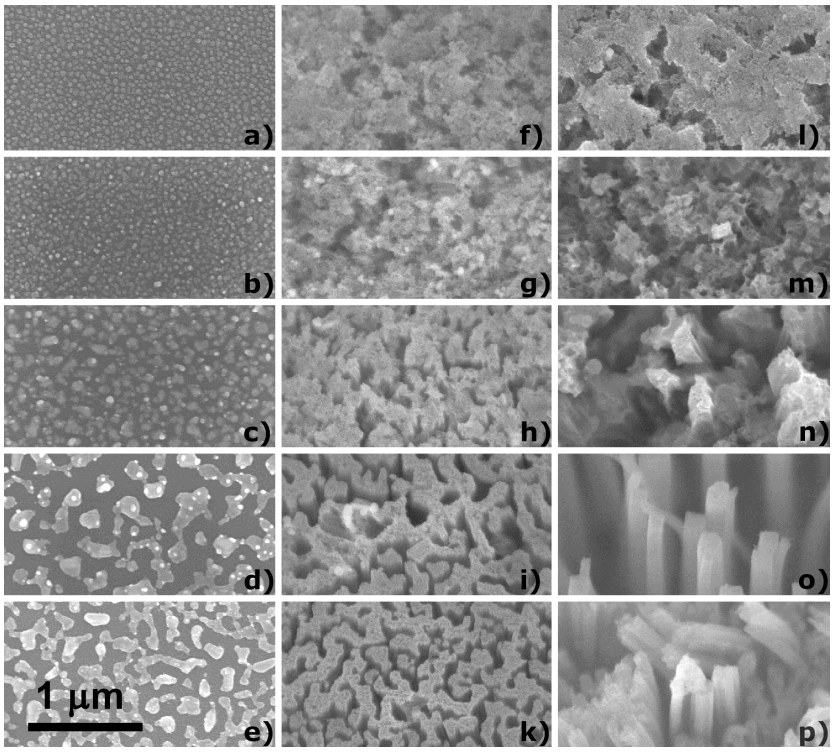

Figure 7: SEM images of porous silicon samples in series B. The columns from left to right are of silver after annealing (left, a to e), after MACE of series B1 (center, f to k), and B2 (right, l to p). The rows from top to bottom correspond to the silver samples with a thickness of 5, 10, 15, 20, and 30 nm.

and silicon.

3.3 Nano-pillar silicon

Changing the preparation conditions to get SHS in previous sections showed that it is possible to select suitable MACE parameters at which the surface morphology of the silicon surface is replicated from that of the original silver layer (Figure 7i and 7k). This result led us to a remark, if we can create a silver layer on the silicon surface, then by etching with suitable conditions, we can make some patterns to obtain nanopillars of silicon, which is the basis for the fabrication results of silicon nanopillars presented in the following.

Controlling MACE conditions allows us to replicate the silver patterns as shown in SEM images (Figure 8), which depict the surfaces at different fabrication steps described in Figure 1. We prepared PS nanoparticles with 500 and 800 nm sizes, which are self-assembled to a nearly close-packed structure. Then, the samples were etched under an oxygen plasma chamber, which made the PS

nanoparticles smaller. So the PS nanoparticles could not keep the structure but were randomly distributed on the silicon surface. Next, a silver layer was coated by thermal evaporation on the etched PS nanoparticles. The silver-coated PS nanoparticles were then removed by dipping them in a cyclohexane solution. Thus, a continuous silver layer with randomly distributed circular holes can be observed. The size of these holes was smaller than that of PS nanoparticles after being etched by oxygen plasma. The etched nanoparticles' random distribution determined the holes' random arrangement. Silver atoms' arrival in the evaporation process could make a certain angle of inclination to the surface. So that silver can be coated on the surface covered by the PS nanoparticles, which led to the uncoated area being smaller than the size of the PS nanoparticles. Finally, after the MACE etching process with a H_2O_2 concentration of 0.12 M, the uncoated circular holes on the silicon surface were converted into silicon nanopillars, as illustrated in last row SEM micrographs of Figure 8.

To maintain the ordered structure of PS nanoparticles, we immobilized them by heating them immediately after the self-assembling process at a temperature of 100°C for 20 min. The results illustrated in Figure 9 show that the hexagonal close-pack arrangement of PS nanoparticles was preserved, although the size has significantly reduced. Meanwhile, the unheated silicon nanopillars are arranged randomly. The contact angle on that silicon nanopillars got the highest value of 164° in our samples. This fact comes from a combination of the silicon nanopillars and the non-polar nature of the silicon surface.

For a hexagonal closed-pack network of nanopillar, the solid-liquid area fraction appeared in (2) is given by

$$f = \frac{\pi}{2\sqrt{3}} \frac{a^2}{b^2} \tag{3}$$

with a is the nanopillar diameter, and b is the average distace between nanopillars. For a flat surface, the Young contact angle θ (in Equation 2) is about 88° for silicon and reduces to 20° for silica [37, 38]. By taking the measure θ_{CB}, which is the tangent angle of the water droplet contour at the contact point with the SHS [36], we deduced the solid–liquid fraction f is 0.024 and 0.013 for silicon and silica surfaces, respectively [21]. From the above calculation, the "apparent" diameter of nanopillars has to be about 19 nm (for silicon) or 10 nm (for silicon native oxide) if the distance between nanopillars is 800 nm, which is the initial size of PS nanospheres. These values are much smaller than the size of nanopillars, about $200 - 300$ nm, measured by SEM micrographs shown in Figure 9. The nanopillars' surface can explain that this result is not flat but nanostructured. Superhydrophobicity in our sample comes from the structure's extrinsic morphology, which consists of the nanopillars with a length of 1 to 2 μm. The air layer between water and SHS must be stable for total internal reflection, requiring the nanopillars to be prolonged. Therefore, series C is suitable for producing the best SHS. There is still a limit because they require many preparation steps. Therefore, further study to simplify the procedures is on the way.

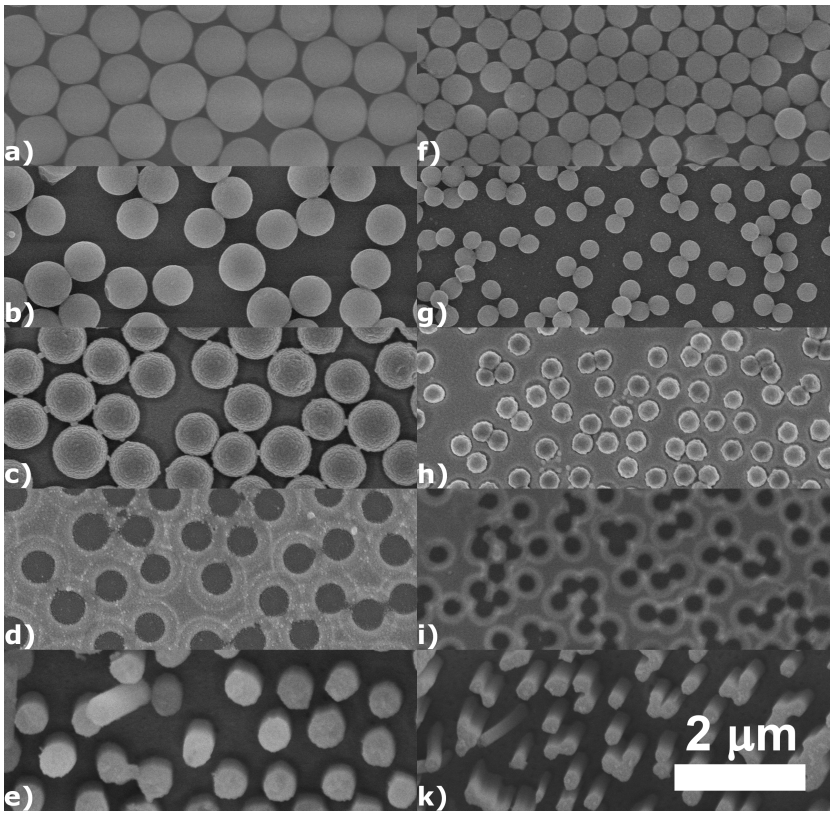

Figure 8: SEM images of nanopillar silicon after different steps of series C1 (right, a to e) and C2 (left, f to k). From top to bottom: (a, f) self-assembling of PS nanoparticles, (b, g) PS nanoparticles after being etched by O_2 plasma, (c, h) after silver deposition, after PS nanoparticles liftoff, (d, i) and (e) after 100 min, (k) 60 min of MACE.

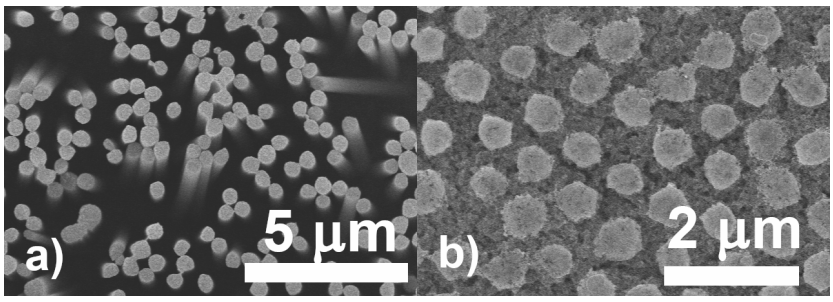

Figure 9: Nanopillars of silicon produced from PS nanoparticles with a diameter of 800 nm (silver layer of 100 nm, oxygen plasma time of 20 min, 60 min of MACE): (a) silicon nanopillars without heating, (b) silicon nanopillars with heating.

4 Conclusion

This paper presents three methods to produce porous PMMA, porous silicon, and nanopillar silicon, which have SHS for a total internal reflection effect at the interface between water and the solid surface. The selective polymer etching to fabricate porous PMMA can only create a hydrophobic surface but is versatile and can be applied to any surface. In contrast, with optimized preparation conditions to fabricate nanostructured silicon, the MACE method is even more complicated but can create highly superhydrophobic surfaces with a water contact angle of 164°. Especially the methods can control the air layer thickness, which is essential for the total internal reflection effect. The materials can be potential for the applications for liquid light guides.

References

[1] Malcolm E. Schrader. Young-dupre revisited. *Langmuir*, 11(9):3585–3589, 09 1995.

[2] A. B. D. Cassie and S. Baxter. Wettability of porous surfaces. *Transactions of the Faraday Society*, 40(0):546–551, 1944.

[3] Sumit Parvate, Prakhar Dixit, and Sujay Chattopadhyay. Superhydrophobic surfaces: Insights from theory and experiment. *The Journal of Physical Chemistry B*, 124(8):1323–1360, 2020.

[4] Bharat Bhushan and Yong Chae Jung. Natural and biomimetic artificial surfaces for superhydrophobicity, self-cleaning, low adhesion, and drag reduction. *Progress in Materials Science*, 56(1):1–108, 2011.

[5] Nenad Miljkovic and Evelyn N. Wang. Condensation heat transfer on superhydrophobic surfaces. *MRS Bulletin*, 38(5):397–406, 2013.

[6] Zhiguang Guo and Weimin Liu. Biomimic from the superhydrophobic plant leaves in nature: Binary structure and unitary structure. *Plant Science*, 172(6):1103–1112, 2007.

[7] Michael Nosonovsky and Bharat Bhushan. *Lotus Versus Rose: Biomimetic Surface Effects*, pages 25–40. Springer Berlin Heidelberg, Berlin, Heidelberg, 2012.

[8] Mingjie Liu, Shutao Wang, and Lei Jiang. Nature-inspired superwettability systems. *Nature Reviews Materials*, 2(7):17036, 2017.

[9] Frank Schellenberger, Noemí Encinas, Doris Vollmer, and Hans-Jürgen Butt. How water advances on superhydrophobic surfaces. *Physical Review Letters*, 116(9):096101–, 2016.

[10] Zhongjia Huang, Sai Yang, Hui Zhang, Meng Zhang, and Wei Cao. Replication of leaf surface structures for light harvesting. *Scientific Reports*, 5(1):14281, 2015.

[11] Samira Shiri and James C. Bird. Heat exchange between a bouncing drop and a superhydrophobic substrate. *Proceedings of the National Academy of Sciences*, 114(27):6930–6935, 2017.

[12] Berna Yalizay, Yagiz Morova, Koray Dincer, Yaprak Ozbakir, Alexandr Jonas, Can Erkey, Alper Kiraz, and Selcuk Akturk. Versatile liquid-core optofluidic waveguides fabricated in hydrophobic silica aerogels by femtosecond-laser ablation. *Optical Materials*, 47:478–483, 2015.

[13] Ke Du, Ishan Wathuthanthri, Junjun Ding, and Chang-Hwan Choi. Superhydrophobic waveguide: Liquid-core air-cladding waveguide platform for optofluidics. *Applied Physics Letters*, 113(14):143701, 2018.

[14] Nguyen Tran Thuat, Hoang Chi Hieu, Ho Duc Quan, Nguyen Quang Quan, and Nguyen Hoang Hai. Focusing lens coupled with optical fiber and sunlight receiving devices using these lenses. Patent US20180094786A1, VNU University of Science, 2018.

[15] Nguyen Tran Thuat and Nguyen Hoang Hai. Solar light receiver using liquid. Patent VN 1-2019-03057, VNU University of Science, 2022.

[16] Henrikki Mertaniemi, Antti Laukkanen, Jan-Erik Teirfolk, Olli Ikkala, and Robin H. A. Ras. Functionalized porous microparticles of nanofibrillated cellulose for biomimetic hierarchically structured superhydrophobic surfaces. *RSC Advances*, 2(7):2882–2886, 2012.

[17] Hee Han, Zhipeng Huang, and Woo Lee. Metal-assisted chemical etching of silicon and nanotechnology applications. *Nano Today*, 9(3):271–304, 2014.

[18] X. Li and P. W. Bohn. Metal-assisted chemical etching in HF/H_2O_2 produces porous silicon. *Applied Physics Letters*, 77(16):2572–2574, 2000.

[19] Peter Dress and Hilmar Franke. Optical fiber with a liquid h2o core. *Integrated Optics and Microstructures III*, 2686:157–163, 1996.

[20] Youfa Zhang, Dengteng Ge, and Shu Yang. Spray-coating of superhydrophobic aluminum alloys with enhanced mechanical robustness. *Journal of Colloid and Interface Science*, 423:101–107, 2014.

[21] Hiroshi Yabu and Masatsugu Shimomura. Single-step fabrication of transparent superhydrophobic porous polymer films. *Chemistry of Materials*, 17(21):5231–5234, 2005.

[22] Pavel A. Levkin, Frantisek Svec, and Jean M.J. Fréchet. Porous polymer coatings: A versatile approach to superhydrophobic surfaces. *Advanced Functional Materials*, 19(12):1993–1998, 2009.

[23] H. Yıldırım Erbil, A. Levent Demirel, Yonca Avcı, and Olcay Mert. Transformation of a simple plastic into a superhydrophobic surface. *Science*, 299(5611):1377–1380, 2003.

[24] Ying Ma, Xinyu Cao, Xinjian Feng, Yongmei Ma, and Hong Zou. Fabrication of super-hydrophobic film from pmma with intrinsic water contact angle below 90 °. *Polymer*, 48(26):7455–7460, 2007.

[25] X. Li and P. W. Bohn. Metal-assisted chemical etching in hf/h2o2 produces porous silicon. *Applied Physics Letters*, 77(16):2572–2574, 2000.

[26] Hee Han, Zhipeng Huang, and Woo Lee. Metal-assisted chemical etching of silicon and nanotechnology applications. *Nano Today*, 9(3):271–304, 2014.

[27] Chenlong Zhang, Sandra Cvetanovic, and Joshua M. Pearce. Fabricating ordered 2-d nano-structured arrays using nanosphere lithography. *MethodsX*, 4:229–242, 2017.

[28] Stefan Walheim, Erik Schäffer, Jürgen Mlynek, and Ullrich Steiner. Nanophase-separated polymer films as high-performance antireflection coatings. *Science*, 283(5401):520–522, 1999.

[29] Tien Van Nguyen, Linh The Pham, Khuyen Xuan Bui, Lien Ha Thi Nghiem, Nghia Trong Nguyen, Duong Vu, Hoa Quang Do, Lam Dinh Vu, and Hue Minh Nguyen. Size Determination of Polystyrene Sub-Microspheres Using Transmission Spectroscopy. *Applied Sciences*, 10(15):5232, 2020.

[30] Kanakaraj Rajkumar, Ramanathaswamy Pandian, Amirthapandian Sankarakumar, and Ramasamy Thangavelu Rajendra Kumar. Engineering silicon to porous silicon and silicon nanowires by metal-assisted chemical etching: Role of Ag size and electron-scavenging rate on morphology control and mechanism. *ACS Omega*, 2(8):4540–4547, 2017.

[31] A. S. Dimitrov, P. A. Kralchevsky, A. D. Nikolov, Hideaki Noshi, and Mutsuo Matsumoto. Contact angle measurements with sessile drops and bubbles. *Journal of Colloid And Interface Science*, 145(1):279–282, 1991.

[32] S. W. Rienstra. The shape of a sessile drop for small and large surface tension. *Journal of Engineering Mathematics*, 24(3):193–202, 1990.

[33] F. K. Skinner, Y. Rotenberg, and A. W. Neumann. Contact angle measurements from the contact diameter of sessile drops by means of a modified axisymmetric drop shape analysis. *Journal of Colloid And Interface Science*, 130(1):25–34, 1989.

[34] C. Huh and R. L. Reed. A method for estimating interfacial tensions and contact angles from sessile and pendant drop shapes. *Journal of Colloid And Interface Science*, 91(2):472–484, 1983.

[35] Yi-Lin Hung, Yao-Yuan Chang, Meng-Jiy Wang, and Shi-Yow Lin. A simple method for measuring the superhydrophobic contact angle with high accuracy. *Review of Scientific Instruments*, 81(6):065105, 2010.

[36] Aurélien F. Stalder, Tobias Melchior, Michael Müller, Daniel Sage, Thierry Blu, and Michael Unser. Low-bond axisymmetric drop shape analysis for surface tension and contact angle measurements of sessile drops. *Colloids and Surfaces A: Physicochemical and Engineering Aspects*, 364(1-3):72–81, 2010.

[37] Murat Barisik and Ali Beskok. Wetting characterisation of silicon (1,0,0) surface. *Molecular Simulation*, 39(9):700–709, 2013.

[38] Paweł Bryk, Emil Korczeniewski, Grzegorz S. Szymański, Piotr Kowalczyk, Konrad Terpiłowski, and Artur P. Terzyk. What Is the Value of Water Contact Angle on Silicon? *Materials*, 13(7):1554, 2020.